

Superresolved Imaging Based on Spatiotemporal Wave-Front Shaping

Guillaume Noetinger¹, Samuel Métails,² Geoffroy Lerosey,³ Mathias Fink,¹ Sébastien M. Popoff,¹ and Fabrice Lemoult^{1,*}

¹*Institut Langevin, ESPCI Paris, Université PSL, CNRS, Paris 75005, France*

²*Aix Marseille Université, CNRS, Centrale Marseille, Institut Fresnel, Marseille, France*

³*Greenerwave, Paris 75002, France*

 (Received 20 September 2022; revised 9 December 2022; accepted 23 December 2022; published 10 February 2023)

A label-free approach to improving the performances of confocal scanning imaging is proposed. We experimentally demonstrate its feasibility using acoustic waves. It relies on a way to encode spatial information using the temporal dimension. By moving an emitter, used to insonify an object, along a circular path, we create a temporally modulated wavefield. Because of the symmetries of the problem, the spatiotemporal input field can be decomposed into harmonics corresponding to different spatial vortices. Acquiring the back-reflected waves with receivers that are also rotating, multiple images of the same object with different point spread functions are obtained. Not only is the resolution improved compared to a standard confocal configuration, but the accumulation of information also allows the building of images that beat the diffraction limit.

DOI: [10.1103/PhysRevApplied.19.024032](https://doi.org/10.1103/PhysRevApplied.19.024032)

I. INTRODUCTION

Imaging devices exploit waves to retrieve information about an object. Ultrasound imaging devices or optical microscopes are two widespread commercially available technologies relying on different waves, both offering key insights for medical diagnosis and scientific research. While having different properties, those approaches rely on the same principles, and their resolution is limited by the same diffraction effects to a distance of the order of the wavelength. More specifically, in optical full-field microscopy, a sample is uniformly illuminated and the waves scattered off an object are collected with a microscope objective. The finite aperture of the optical system filters out waves corresponding to high scattering angles and thus the smaller details [1]. The image of a point, i.e., the point-spread function (PSF) of the system, is an Airy spot whose first zero is located at a distance $1.22\lambda/(2\text{ NA})$ from the focus (where λ is the operating wavelength and NA the numerical aperture). The Rayleigh criterion states that two pointlike objects closer than this distance cannot be distinguished [2].

Overcoming this limitation is the domain of *superresolution* imaging and many techniques have already been proposed [3–12]. Although techniques involving fluorescent labels allow building images with a resolution much smaller than the diffraction limit, they are burdensome and sometimes toxic to cells. Achieving superresolution in the far field without any labels still remains an important

challenge of modern physics [4] with numerous applications. As any label-free imaging scheme can be decomposed into two main steps, i.e., acquiring data and processing the acquired data, those techniques can be divided in two different classes.

The first strategy consists in shaping the illumination and/or the collection of waves. The simplest implementation is the well-known confocal microscope [13,14], where an illumination pattern is projected to an object and the backscattered waves from a diffraction-limited volume are collected. The object is scanned to build an image Im that is the convolution of the object Obj and the product of the illumination and collection PSFs [15]:

$$\text{Im} = \text{Obj} \otimes (\text{PSF}_{\text{ill}} \cdot \text{PSF}_{\text{coll}}). \quad (1)$$

In addition to suppressing out-of-focus signals, it enhances the maximum transmitted spatial frequency by a factor of 2 [15]. As in diffractive tomography [16], the accessible Fourier space, i.e., the *Ewald sphere*, is now given by the sum of wave vectors $\mathbf{k}_{\text{ill}} + \mathbf{k}_{\text{coll}}$ respectively associated with the illumination \mathbf{k}_{ill} and collection \mathbf{k}_{coll} wave vectors. Nevertheless, such improvement is difficult to observe experimentally due to a poor gain for high spatial frequencies. The increase in lateral resolution is usually considered to be of the order of roughly 40%. Other approaches were proposed, all relying on engineering the illumination or the collection scheme, such as diffractive tomography [16,17], ptychography [18], structured illumination [19], or other PSF engineering [20,21]. However, all these techniques ultimately remain limited in resolution by the diffraction.

*fabrice.lemoult@espci.psl.eu

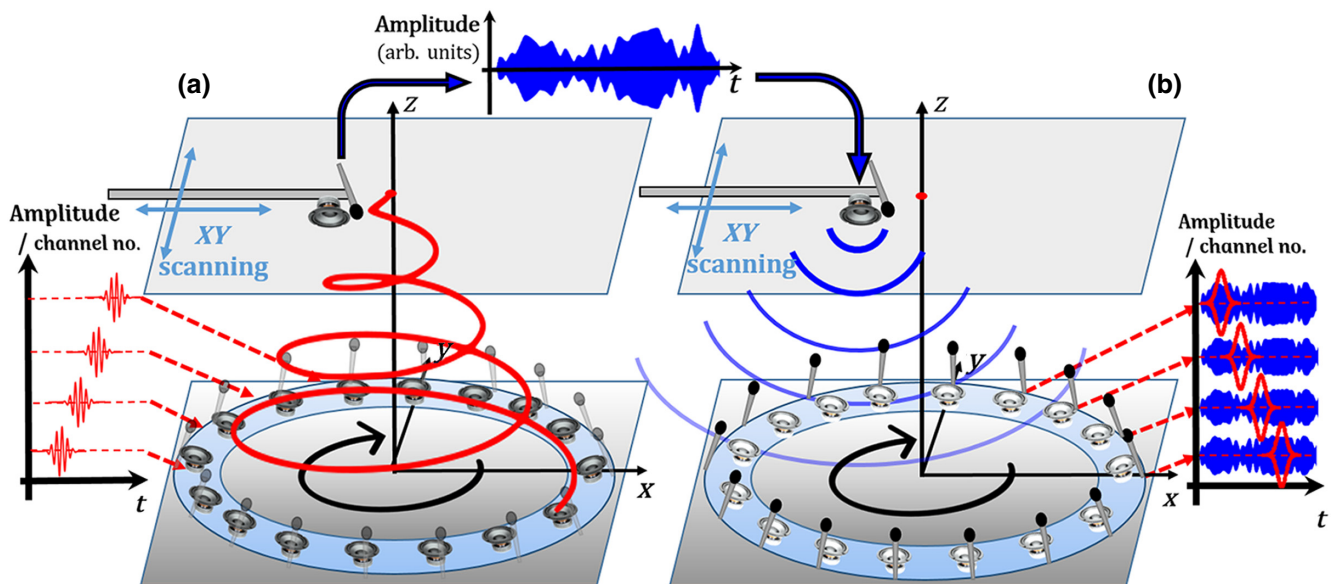


FIG. 1. Acoustic experimental setup. (a) Loudspeakers emit successively to mimic a single rotating loudspeaker. The pressure field is recorded in a focal plane by a microphone on a translation stage. (b) The recorded field is sent back by a loudspeaker next to the microphone. This is equivalent to reflection by a point scatterer. The backscattered field is recorded by microphones to mimic a rotating receiver by properly time gating and summing all the signals.

The second strategy consists in developing algorithms for reconstructing the image. Indeed, the Rayleigh criterion is somewhat of an arbitrary rule. In particular, it assumes that any spatial frequency outside of the transmitted bandwidth is definitely lost. Nonetheless, strong arguments exist to claim that the resolution can be limited only by the signal-to-noise ratio [22,23]. However, the presence of noise in real-life experiments makes the problem ill-posed, forbidding a direct inversion of the mathematical equations. Various algorithms were developed to regularize the system by compensating for unknown or noisy information using strong priors [24–27].

In this paper, we propose to investigate the effect of a time-varying pupil of the confocal microscope. Thanks to the scanning process, Eq. (1) remains valid if PSF_{III} becomes time dependent. We use this property to harvest more information from the object with a well-chosen illumination sequence. Our approach combines wave-front shaping and mathematical deconvolution for improving the resolution. It consists in using dynamic wave-front shaping to rotate an illumination wave front, thus using the temporal domain as an additional way to encode information. We show that it is equivalent to measuring the image of an object with multiple imaging systems with different orthogonal PSFs, corresponding to different harmonics of the received signals. The addition of information provided by those images allows increasing the effective signal-to-noise ratio and thus improving the resolution without any particular assumption on the sample. We experimentally demonstrate this concept in acoustics in a confocallike configuration by reconstructing the image of

two small scatterers. Using a simple deconvolution process, we show that two scatterers can be distinguished below the diffraction limit.

II. EXPERIMENTAL DETAILS AND RESULTS

The fundamental idea of the proposal relies on creating a singularity that will allow precisely discriminating one point from the rest of the object. Pointlike scatterers at different positions will perceive different time modulations, depending on their distance to the rotation axis. Only a scatterer located exactly on the rotation axis backscatters an unmodulated wave. This modulation can also be understood using the Doppler effect: in the rotating frame, the object Doppler shifts the waves. Interestingly, as the rotation comes periodically to the same position, everything is actually encoded as a periodic modulation on an initial monochromatic excitation.

To access the temporal field, we implement this concept with audible acoustic waves, but the same framework can be transposed to other wave-based imaging systems, such as optical microscopes. In order to generate a rotating source, we place a set of 16 loudspeakers and microphones on a 55-cm-radius circle. Each of them is connected to a multichannel Antelope Orion32+ soundboard (see Fig. 1) controlled through a computer. The speakers sequentially emit time-gated monochromatic signals in such a way that it is equivalent to having a rotating source emitting a monochromatic signal at a frequency $\omega_0 = 1600$ Hz (equivalent to a wavelength of 21.4 cm).

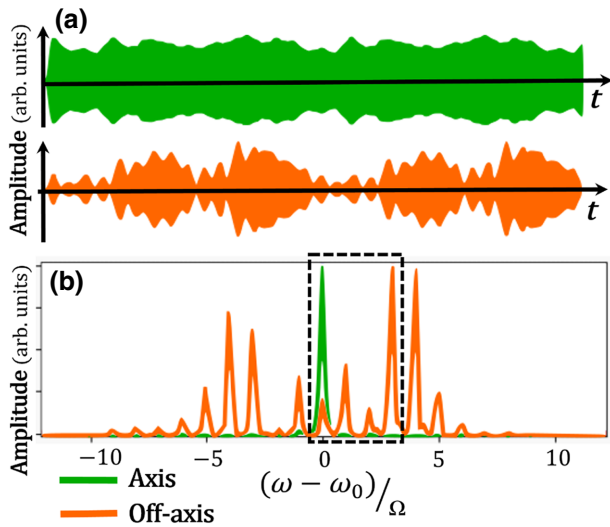


FIG. 2. Temporal signals and spectra. (a) Backscattered signals for a scatterer on the rotation axis (top) and off-axis (bottom). (b) Spectrum of the signals; the on-axis signal is almost monochromatic while the off-axis one presents peaks at each harmonic $\omega_0 + n\Omega$.

This has the advantage of not requiring any physical rotation. The rotation angular frequency $\Omega = 4$ Hz is chosen so that the speed of the rotating emitter is low compared to the wave velocity. A microphone placed on a translation stage records the acoustic field in a plane (hereinafter called the *focal plane*) located 1.7 m above the speakers.

To mimic a pointlike scatterer, a microphone and a loudspeaker are used to record the signal at a target position in the focal plane and then reemit the recorded signal (Fig. 1). The microphones arranged in a circle then measure the backscattered field. Finally, the recorded signals are time gated and summed to mimic a rotating detector (see Appendix B for experimental details). We first show the transient backscattered signals of a scatterer located on and outside the rotation axis in the focal plane (Fig. 2). As expected, the spectrum of the signal corresponding to the scatterer on the axis appears to be almost monochromatic. On the contrary, the signal for the off-axis scatterer displays a periodic temporal modulation of its envelope. In the Fourier space, this corresponds to a frequency comb centered around ω_0 with a spacing between peaks corresponding to the rotation frequency Ω [Fig. 2(b)]. This effect is actually well known in the telecommunication community: it is similar to the phase shift observed in frequency modulation (FM) radio [28]. Indeed, the spectrum of FM radio is also known to be a frequency comb centered on the carrier frequency with a spacing equal to the modulation frequency (see Appendix A).

Similarly, all the transient signals in this experiment display a periodic modulation, and from now on, only the data corresponding to the different harmonics $\omega_0 + n\Omega$ with

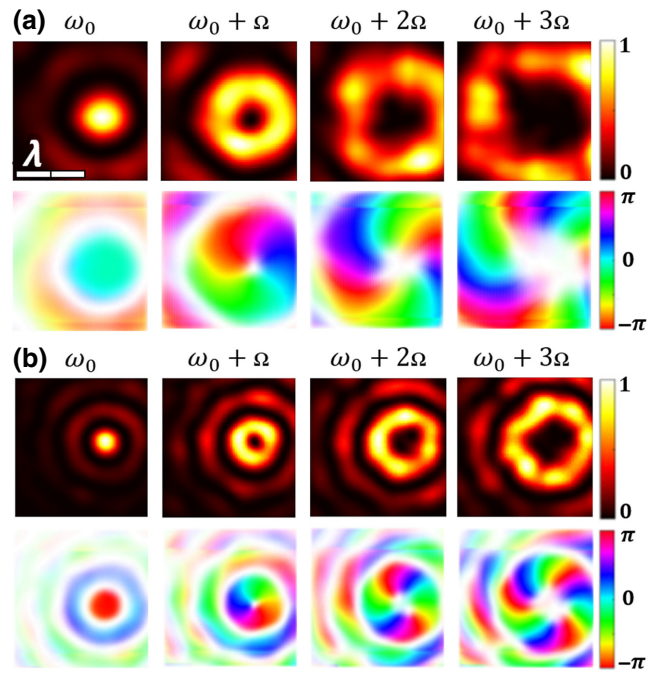


FIG. 3. Map of the field at each frequency $\omega_0 + n\Omega$. (a) Field in the focal plane for $n \in \llbracket 0; 3 \rrbracket$. (b) Backscattered signals. For each dataset, the first row corresponds to the intensity and the bottom row is the phase (weighted by the amplitude).

$n \in \mathbb{Z}$ are displayed. After this temporal Fourier transform the rotation frequency Ω plays no role. What matters is the presence of this periodic modulation regardless of its frequency. An important consequence of this is that we could obtain the same effect with any waves, for instance with light.

To investigate the imaging capabilities of our system, a full scan of the focal plane is performed. The field in the focal plane as well as the backscattered signals are recorded. The spatiotemporal signals are then projected onto the different harmonics. The maps of the complex field in the focal plane corresponding to the harmonics in the range $\llbracket 0; 3 \rrbracket$ are represented in Fig. 3(a).

The field at harmonic $n = 0$, or, equivalently, at the initial carrier frequency ω_0 [left column of Fig. 3(a)], reveals a focal spot at the central position. Its width is approximately 1.3λ . It corresponds to the diffraction-limited focal spot that would be obtained through a thin ring aperture of $\text{NA} = 0.31$ illuminated by a monochromatic wave at ω_0 . Reciprocally, it is the PSF of a full-field microscope with a thin ring aperture, with a first zero at a distance $l_{\text{res}} = 0.76(\lambda)/(2 \text{NA}) = 28$ cm from the focal spot (see Appendix C). The field at the harmonic n is a vortex of topological charge n and is concentrated on a ring whose radius increases with $|n|$. This is consistent with the calculations in FM radio telecommunication (see Appendix A)

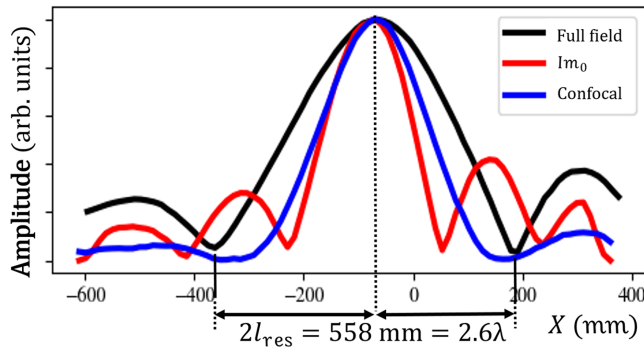


FIG. 4. Experimental amplitude profiles (in absolute value) of the full-field PSF, the confocal PSF, and PSF_0 , the point-spread function at ω_0 in the dynamic case. The zeros of PSF_0 seem approximately 2 times closer to the origin compared to the two other scenarios.

that permits us to write this field as

$$\sum_{n=-\infty}^{\infty} J_n \left(2\pi \frac{Rr}{\lambda z} \right) e^{in\theta} e^{i(\omega_0 + n\Omega)t}. \quad (2)$$

As expected, the central point on the rotation axis acts as a singularity. Similarly to the field at ω_0 , they are equivalent to the PSF of a full-field acoustical microscope with a thin ring aperture on which a vortex plate would have been added. This matches with numerical calculations (see Appendix D).

The images corresponding to the first harmonics of the backscattered signals are also represented [Fig. 3(b)]. They resemble to the maps in the focal plane and all exhibit similar vortices. However, there is a homothety relationship between the two sets of images so that the rings corresponding to the maximum of intensity at each harmonic have a radius diminished by the same factor 2 that can also be seen in the transient fields (see Appendix B). To highlight the reduction in the width of the PSF in the backscattered signals, we show in Fig. 4 a cross view of the PSFs at ω_0 . We compare the field in the focal plane (equivalent to a full-field configuration [29]) in the backscattered field. The position of the first zero confirms this improvement by a factor of 2. Compared to a confocal configuration where the PSF is the square of that in the focal plane, the side lobes are higher but the main one is narrower.

We interpret this effect as a consequence of the dynamic configuration used in this experiment similar to the doubling of the spatial frequency support obtained in structured illumination microscopy [19] or diffractive tomography [16]. During a rotating acquisition the loudspeakers on the illumination pupil send waves associated with the wave vectors corresponding to the highest numerical aperture allowed by diffraction. This means that $\|\mathbf{k}_{\text{ill}}\| =$

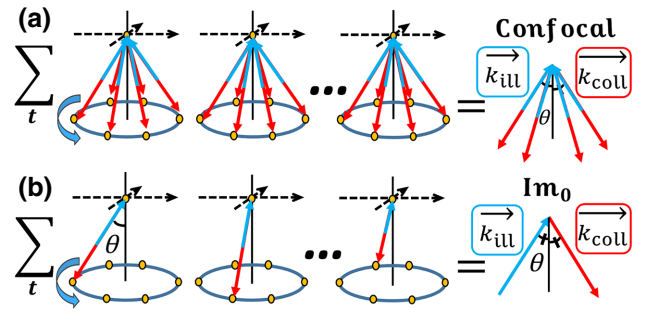


FIG. 5. Explanations of the resolution enhancement with an annular acoustic lens made of six lenses and microphones. (a) Construction of the confocal images. Using the temporal Fourier transform and keeping the image at the carrier frequency is equivalent to calculating the temporal sum of the signals up to a proportionality factor. (b) Construction of Im_0 with dynamic signals.

$2\pi \text{NA}/\lambda = k_{\text{max}}$; then the rotating microphone also collects waves with $\|\mathbf{k}_{\text{coll}}\| = k_{\text{max}}$. In the presented experimental scheme, the two wave vectors are always colinear at any time. As a consequence, the wave vectors sum constructively in Fourier space: in the image the wave vectors are located on the circle $\|\mathbf{k}_{\text{ill}} + \mathbf{k}_{\text{coll}}\| = 2k_{\text{max}}$. The rotating emission (reception) filter applied to mimic a rotating emitter (receiver) is in fact an optimal spatiotemporal filter [30] to select those wave vectors as shown in Fig. 5.

The next step consists in harnessing the diversity of signals offered by the dynamic nature of the process to improve the imaging resolution below the diffraction limit. Our apparatus is equivalent to a confocal microscope in a monochromatic highly coherent configuration, except that the illumination pattern is modulated periodically in time. As a result, the object information is encoded in the different harmonic frequencies. Consequently, we

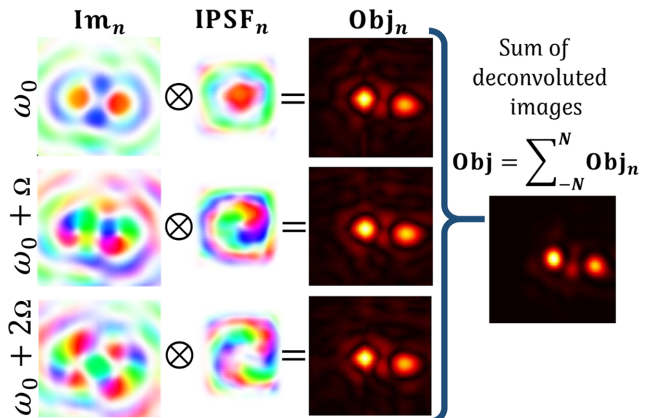


FIG. 6. Deconvolution procedure. The images at each harmonic are convolved with a regularized inverse of the PSF_n . All the independent reconstructions are summed to give a final sharp image.

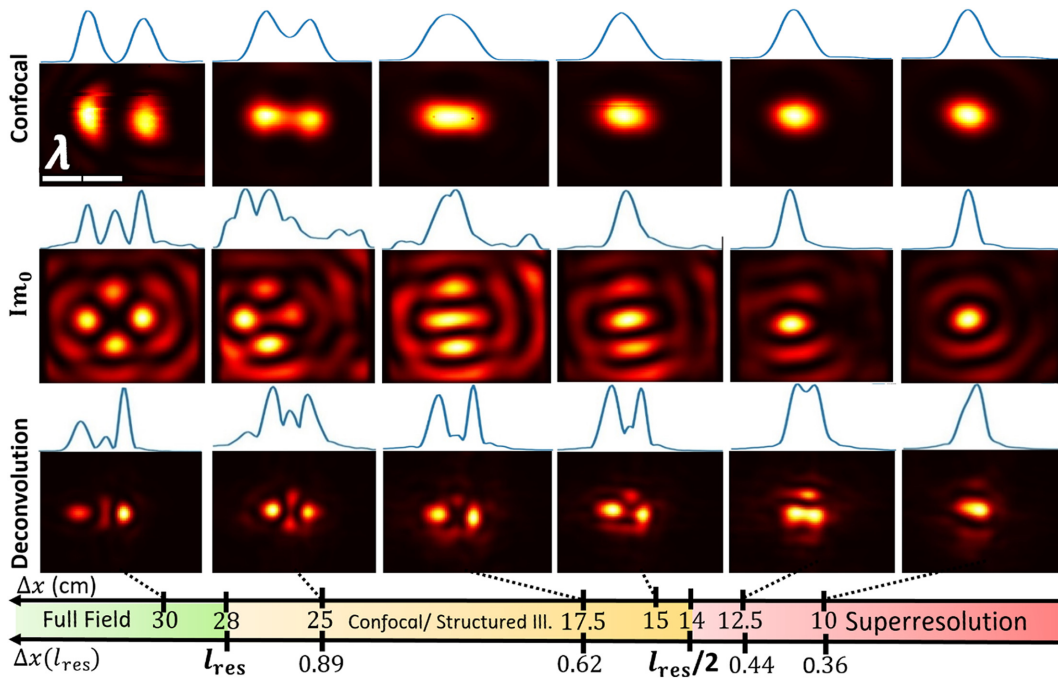


FIG. 7. Quantification of the resolution limit of the system. Two emitters in the focal plane are imaged. Images are shown in normalized intensity and the maximum profile on the separation axis (X) is shown above each image. Comparison between the confocal images (top row), dynamic images at ω_0 (middle row), and the deconvoluted dynamic images (bottom). Close to $l_{\text{res}}/2$, the confocal setup fails to distinguish two diffusers. With the deconvolution process, the two pointlike objects are made distinguishable further from this limit.

obtain as many images $\text{Im}_n(x, y)$ as the number of measured harmonic frequencies. Each of the images is also the convolution product between the object and the point spread function $\text{PSF}_n(x, y)$, which is specific to the harmonic n , and corresponds to a diffraction-limited vortex of vorticity n . As two vortices with different topological charges are orthogonal, each channel carries partially different information about the object. Moreover, thanks to the reduced apparent wavelength previously observed in the backscattered PSFs, the resolution is increased.

The images Im_n corresponding to two point scatterers separated by 30 cm are acquired. The images of the first harmonics are displayed on the left of Fig. 6 as color coded images of their phase. Each of them shows a vortex centered on each scatterer with a topological charge that corresponds to the considered harmonic.

For each harmonic, a deconvolution is needed in order to obtain an image of the two scatterers. This consists in convolving the images by the inverse IPSF $_n$ of the point-spread function PSF_n as depicted in Fig. 6. Such an inverse is calculated from the experimental PSF_n obtained with a single emitter in the spatial Fourier domain as it only involves dot products. To be robust to the presence of noise, a Tikhonov regularization [31–33] is achieved. Each pseudoinverse operator reads (see Appendix E)

$$\widehat{\text{IPSF}}_n = (\widehat{\text{PSF}}_n^* \cdot \widehat{\text{PSF}}_n + \sigma)^{-1} \cdot \widehat{\text{PSF}}_n^*, \quad (3)$$

where σ corresponds to the noise-to-signal ratio, the asterisk denotes the complex conjugate, and the “hat” symbol denotes the two-dimensional spatial Fourier transform. Note that in real space, the inverse IPSF $_n$ exhibits a vorticity with a charge opposite to that of PSF_n .

By deconvolution, each harmonic provides its own intensity image of the two scatterers. The last step consists in summing all the images from harmonic -4 to 4 and a final image is built (right-hand side of Fig. 6). The signals add up and the average noise decreases, leading to a cleaner final image of the two scatterers.

We then change the distance between the two scatterers to find when it becomes impossible to distinguish them (Fig. 7). For the sake of comparison, *classical confocal images* are also acquired (see Appendix C). These images reveal that the scatterers cannot be resolved when their distance is less than 22 cm ($\simeq \lambda = 0.79l_{\text{res}}$, corresponding to 30% of the diffraction limit). The images at harmonic $n = 0$ (central row) show smaller spatial variations but a high level of artifacts not allowing one to distinguish any objects. When taking into account all the available harmonics and their inversion procedure, it is possible to beat the Rayleigh criterion and reach a resolution of 12.5 cm = 0.58λ . We numerically verify using the experimental PSFs of Fig. 3 and a continuous object that artifacts are not an issue when the sample is not a sparse object (see Appendix E). It corresponds to an improvement

of 70% compared to the confocal configuration and 10% compared to structured illumination ($l_{\text{res}}/2$). Noise remains the limitation: the noise-to-signal ratio parameter σ , estimated at 0.003 in those experiments (see Appendix E), still limits the performance. This is a standard order of magnitude in microscopy [24], and any enhancement would immediately translate into an increase of the resolution capabilities. Moreover, further improvements can be made using smarter algorithms [34,35] where our solution would be used as an initial guess.

III. CONCLUSION

In conclusion, we propose exploiting the time domain as a way to improve the resolution of an imaging device and demonstrate its applicability with an experiment based on audible acoustics. Projecting a time-periodic pattern on a sample allows acquiring multiple images of the same sample with orthogonal PSFs. Using a rotating pattern, those PSFs correspond to vortices with different topological charges. The augmentation of information allows us to beat the diffraction limit, even in the presence of experimental noise. In microscopy, it could offer an easy way to obtain label-free high- or superresolution images.

This strategy could be combined with nonlinear phenomena such as fluorescence saturation involved in nonlinear structured illumination [36].

ACKNOWLEDGMENTS

This work is supported by LABEX WIFI under Grants No. ANR-10-LABX-24 and No. ANR-10-IDEX-0001-02-PSL*, and partially supported by the Simons Foundation/Collaboration on Symmetry-Driven Extreme Wave Phenomena.

APPENDIX A: FIELD OF A ROTATING EMITTER

We consider an emitter emitting a wave at frequency ω_0 , rotating at speed v given by angular frequency on a circle of radius R located in the (x, y) plane and a static receiver at position $(x, 0, z)$. The frequency detuning reads

$$\Delta f = f_r - f_0 \simeq \frac{V(t)}{c} = \frac{\mathbf{u} \cdot \mathbf{v}}{c}, \quad (\text{A1})$$

where $V(t)$ is the projection of the speed of the emitter on the straight line directed by \mathbf{u} the unitary vector directed from the emitter to the receiver. To go further, we need to express the coordinates of the emitter \mathbf{r}_E and receiver \mathbf{r}_R as

$$\begin{aligned} \mathbf{r}_R &= (x, 0, z), \\ \mathbf{r}_E(t) &= (R \cos(\Omega t), R \sin(\Omega t), 0). \end{aligned} \quad (\text{A2})$$

The detuning then reads

$$\Delta f(t) = \frac{f_0}{c} \frac{-Rx\Omega \sin(\Omega t)}{\sqrt{x^2 - 2xR \cos(\Omega t) + R^2 + z^2}}. \quad (\text{A3})$$

We can only consider the phase variation and neglect the amplitude variation; this would be coherent with a far-field approximation. Then

$$\Delta f(t) = \frac{R\Omega x f_0 \sin(\Omega t)}{cz}, \quad (\text{A4})$$

to a minus sign factor. The wave perceived by the receiver can be written as

$$S_r(\mathbf{r}, t) \propto \exp \left\{ i2\pi \int_0^t (f_0 + \Delta f(\mathbf{r}, t)) dt \right\}, \quad (\text{A5})$$

to a multiplicative factor. We now have to express the instantaneous phase of S_r ; since the frequency can be written as $f_0 + \Delta f(\mathbf{r}, t)$, then

$$\begin{aligned} S_r(\mathbf{r}, t) &\propto \exp \left\{ i2\pi \int_0^t \left(f_0 - \frac{R\Omega x f_0}{cz} \sin(\Omega t) \right) dt \right\} \\ &= \exp \left\{ i2\pi \left(f_0 t + \frac{R x f_0}{cz} \cos(\Omega t) \right) \right\}. \end{aligned} \quad (\text{A6})$$

Now the easiest way is to use the generating function of Bessel's functions [37],

$$e^{a(b-1/b)/2} = \sum_{n=-\infty}^{\infty} J_n(a) b^n,$$

where we set $a = 2\pi f_0 A_m(\mathbf{r}) t = 2\pi f_0 R x f_0 t / cz = 2\pi f_0 R x t / \lambda z$ and $b = e^{i\Omega t}$, which gives

$$\frac{b - 1/b}{2} = \frac{e^{i\Omega t} - e^{-i\Omega t}}{2} = i \sin(\Omega t).$$

We changed the cosine into a sine, which is equivalent to a phase shift or a shift of the time axis. We obtain

$$\begin{aligned} S_r(\mathbf{r}, t) &\propto e^{2\pi i f_0 t} \cdot \sum_{n=-\infty}^{\infty} J_n(2\pi f_0 A_m(\mathbf{r})) e^{in\Omega t} \\ &= \sum_{n=-\infty}^{\infty} J_n(2\pi f_0 A_m(\mathbf{r})) e^{i(f_0 + n\Omega)t} \\ &= \sum_{n=-\infty}^{\infty} J_n \left(2\pi f_0 \frac{Rx}{cz} \right) e^{i(f_0 + n\Omega)t} \\ &= \sum_{n=-\infty}^{\infty} J_n \left(2\pi \frac{Rx}{\lambda z} \right) e^{i(f_0 + n\Omega)t}. \end{aligned} \quad (\text{A7})$$

To introduce the angle θ of the receiver, it is simply possible to add a phase at the origin in the detuning

$\Delta f(\mathbf{r}, t) = R\Omega r \sin(\Omega t + \theta)/(\lambda z)$; this gives the final expression

$$S_r(\mathbf{r}, t) \propto \sum_{n=-\infty}^{\infty} J_n\left(2\pi \frac{Rr}{\lambda z}\right) e^{i(f_0 + n\Omega)t + n\theta}. \quad (\text{A8})$$

APPENDIX B: DETAILS OF THE EXPERIMENT

All the experimental protocol and data analysis is carried out using PYTHON.

1. Setup

The soundcard I/O device is an *Antelope Orion TB32+* with a total of 32 output channels and 32 input channels. The sampling frequency is 44 100 kHz. Thanks to the “pyaudio” library live emitting and recording is controlled by computer. The setup is depicted in Fig. 8.

a. Imaging and excitation lenses

Inside an anechoic chamber 16 microphones and loudspeakers are disposed in a circle of radius $R = 55$ cm and connected to the soundcard. The distance between each microphone and loudspeaker is thus approximately $(2\pi/16)R = 21$ cm. This imposes an upper limit on the wavelength used: to have a satisfying spatial sampling of a rotating emitter, this distance should roughly be of the same order of magnitude as the wavelength.

All the microphones are *t.bone MM-1* pressure recording omnidirectional microphones. They are all connected to their own microphone preamp (Antelope MP32) that provides a phantom power supply as well as electronic amplification. All the loudspeakers are 4Ω 3-W loudspeakers equipped with one tunable Adafruit PAM8302 class D 2.5-W mono amplifier each. The amplifiers are

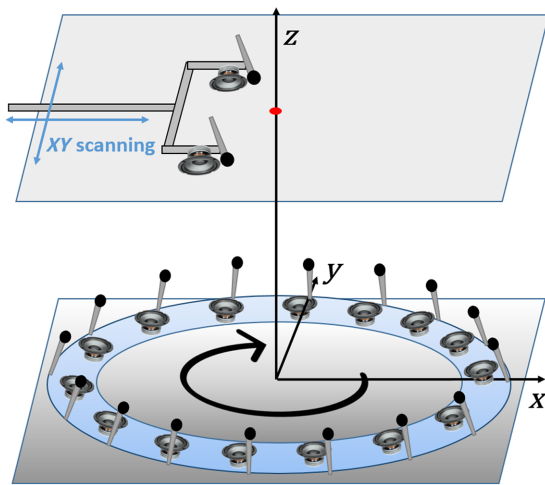


FIG. 8. Sketch of the complete setup. The ring of loudspeakers and microphones and the two scatterers are depicted. The distance between the two scatterers can be adjusted.

connected to an electrical USB 5-V outlet and amplify each output of the soundcard; the amplified and impedance matched signal is delivered to the loudspeakers.

In practice, the microphone are slightly higher than the loudspeakers by approximately 15 cm, leading to a small difference in the numerical aperture for the illumination (loudspeakers) and collection (microphones) lenses $\text{NA}_{\text{ill}} \simeq d/\sqrt{h_{\text{ls}}^2 + d^2} = 0.55/\sqrt{1.72^2 + 0.55^2} = 0.31$ and $\text{NA}_{\text{coll}} \simeq d/\sqrt{h_{\text{mic}}^2 + d^2} = 0.55/\sqrt{1.57^2 + 0.55^2} = 0.33$ that we choose to neglect.

b. Active scatterers

Active scatterers are made with a t.bone MM-1 microphone and a 3-W loudspeaker close together at the sub-wavelength scale; here the centers of the microphone and loudspeaker are slightly less than 2 cm apart. Each active

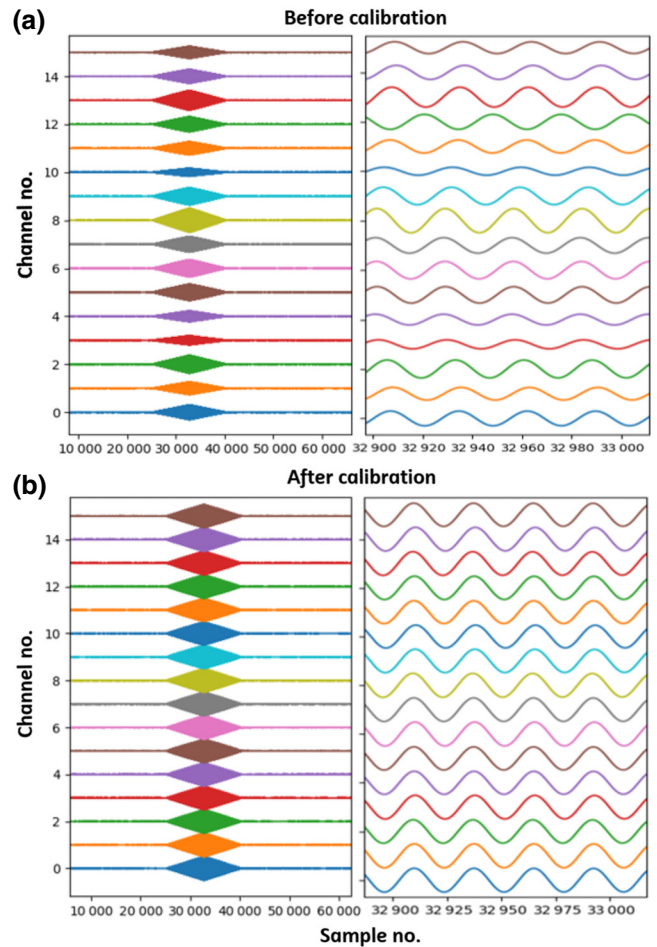


FIG. 9. Calibration procedure. (a) Signals measured in the focal plane before calibration. The signals are recorded on the rotation axis when each lens’s speaker emits a pulse: mismatches in amplitude and phase (as highlighted in the enlarged plot on the right) are evidenced. (b) After calibration. All signals have the same amplitude and phase.

scatterer's loudspeaker is connected to the output of a Dynavox HiFi amplifier. We choose not to use another PAM8302 amplifier as for the lens's amplifier to have a better sound quality for the reflection process inexpensively and a simple knob to set the gain. They are fixed at the end of a beam on the translation stage.

c. Translation stage

The translation stage is a heavy duty two-axis translation stage with two stepper motors powered with a *Schrittmotor CI42* controller interfaced using *pyserial*. Each axis has a total stroke of approximately 1 m that limits the field of view of the experiment. This has to be taken under consideration when choosing the wavelength λ . It should be low enough to allow a few λ of displacement on each axis.

d. Rotating emitter-receiver signal computation

For each channel corresponding to the rotating emitter, a monochromatic signal is multiplied by a Gaussian or triangular window centered on the time corresponding to the angular position of the rotating emitter. The width of this window is such that the sum of all time-gated signals corresponds to the desired emission profile of the rotating loudspeaker that is a constant monochromatic signal here. This imposes the width at half maximum of the windows to be equal to the movement time between each loudspeaker. The same process is achieved for the receiving channels to mimic a rotating receiver.

2. Calibration

All the impedance and gain of the 2.5-W amplifiers are slightly different from one another. This induces random, yet deterministic, amplitude and phase differences in the signal sent for each channel [Fig. 9(a)]. If the same signals are sent simultaneously to every channel, there will be no spatial focusing centered on the rotation axis observed. In order to compensate for this effect, we perform a calibration step before the experiments.

A microphone on the translation stage (corresponding to one of the active scatterers) is put on the rotation axis. Each lens's loudspeaker sends a pulse (monochromatic signal multiplied by a Gaussian window) recorded by the on-axis microphone in the focal plane. The relative height and position of each pulse maximum gives a corrective multiplying factor (gain) and sample shifting (phase) for each channel [Fig. 9(b)]. These correcting factors are next applied to the precomputed signals for each channel. As a consequence, a nice focusing can be observed in the focal plane on the rotation axis if all channels of the lens emit together.

For the experiment with two loudspeakers in the focal plane (used for the active diffusers), the same phenomenon is observed although less pronounced thanks to the higher quality of the amplifier. A similar calibration is performed

nevertheless using the same process with the reference microphone being one microphone of the lens.

It is not necessary to perform the same process for the microphones, given the better quality of both the microphones and the preamplifier.

3. Acquisition process

a. Dynamic configuration

The emission frequency is chosen considering the compromise between the field of view and spacing between the lens's loudspeakers. It is set to 1600 Hz; this corresponds to a wavelength of 21.4 cm. The rotation frequency is set to 4 Hz with the number of turns set to four to allow for averaging. We choose this value of 4 Hz to use a small bandwidth of the audio setup and because the rotation speed $R\Omega$ is small compared to the speed of sound c ; the Doppler effect is then approximately linear. For reconstruction, we consider the signal only in the range $[\omega_0 - 3\Omega, \omega_0 + 3\Omega]$ (see further discussions), corresponding to a spectral width of 28 Hz, small compared to the sampling frequency of 44 100 Hz.

During the acquisition the scatterers are moved point by point with the translation stage on a square grid of side length 90 cm with large temporal pauses for mechanical stability. For each point, the sequence of precomputed signals (namely after calibration) mimicking a rotating source is emitted by the loudspeakers. For the sake of speed, only four cycles are emitted. In the meantime, the wavefield in the focal plane is measured by the microphones of the active scatterers. To erase low-frequency variations and 50-Hz modulation, it is numerically filtered around the emitted frequency with a Butterworth bandpass filter of order 4. The bandwidth of this filter, which has to be large enough to keep the signal with the modulation coming from the rotation, is chosen to be 150 Hz.

The recorded signal is then emitted by the speaker in the focal plane. It is recorded by the lens's microphones and filtered with the same numerical bandpass filter as before. To obtain the signal recorded by a virtually rotating recorder, all the signals are multiplied by the temporally shifted Gaussian windows.

b. Confocal configuration

To perform a confocal image with the same setup, we should emit a monochromatic signal from all the loudspeakers at the same time with the same amplitude and phase (thus requiring the calibration). However, in our case, all the amplifiers cannot send signals at the same time because that would draw too much power from the electrical outlet. We thus apply the superposition theorem to sum all the signals received in the focal plane when each speaker emits a Gaussian pulse. For the receiving part, no temporal windowing is applied and all signals are summed

together. Finally, only the Fourier transform at the angular frequency ω_0 is kept, thus providing the equivalent of a monochromatic experiment.

c. Experiment with two scatterers in the focal plane

The code is the same with two scatterers in the focal plane except during the reemission step. Instead of routing the filtered signal from a single microphone to a single loudspeaker, this has to be achieved for another pair of microphone and loudspeaker.

4. Building images

To build images at frequencies $\omega_0 + n\Omega$ with $n \in \mathbb{N}$ from complex data of shape $[N_x, N_y, N_t]$ corresponding to the number of steps in the x and y directions and the number of samples (typically $[N_x, N_y, N_t] = [80, 80, 44\ 100]$), the data are first demodulated by multiplying each temporal vector (last dimension) with a monochromatic signal at the carrier frequency $e^{-i\omega_0 t}$. Then instead of computing the temporal Fourier transform and extracting the value of this transform at $n\Omega$, we compute the Fourier coefficients for the appropriate n . To do this, we multiply each temporal vector (last dimension) with a monochromatic signal $e^{-in\Omega t}$, sum along this dimension, and normalize by N_t .

APPENDIX C: COMMENTS ON THE RESULTS

1. Full-field resolution

The diffraction-limited focal spot of a full-field microscope with a regular microscope objective (i.e., a full lens) is given by the Fourier transform of the pupil function [38]

$$\text{PSF}(r) \propto \int_0^1 J_0\left(\frac{2\pi \text{NA}}{\lambda} r r'\right) r' dr' \propto \frac{J_1(2\pi \text{NA} r/\lambda)}{2\pi \text{NA} r/\lambda}, \quad (\text{C1})$$

where r' is the normalized integration variable corresponding to the radial contribution of the pupil to the focal spot. The first zero of this function corresponds to $2\pi \text{NA} r/\lambda = 3.8$. According to the Rayleigh criterion the resolution limit is then $l_{\text{res}} = 1.22\lambda/(2 \text{NA})$. In our case the pupil function is a thin ring and thus the PSF reduces to a single element of the previous integral:

$$\text{PSF}(r) \propto J_0\left(\frac{2\pi \text{NA} r}{\lambda}\right). \quad (\text{C2})$$

The first zero of this function corresponds to $2\pi \text{NA} r/\lambda = 2.4$ [37] so $l_{\text{res}} = 0.76\lambda/(2 \text{NA})$; this is equal to 27.1 cm here. The fact that the imaging resolution is given by this criterion comes from reciprocity [29].

Experimentally, this monochromatic configuration corresponds to the wave field measured in the focal plane at the harmonic $n = 0$. A radial profile of the absolute value

of the latter is represented in Fig. 4. The difference in position of the two first zeros corresponding to $2l_{\text{res}}$ is measured (see Fig. 4) and gives $l_{\text{res}} = 27.9 \simeq 28$ cm, which corresponds to the previous calculation.

2. Confocal resolution

When performing a confocal scenario, the wavefield is focused during the emission and the reception step. As a consequence, the round trip implies a squaring of the full-field PSF. Experimentally, the confocal image is obtained after a full scan of the focal plane by the scatterer. Again, a radial profile of the absolute value of the confocal PSF is shown in Fig. 4. The zeros of the confocal experiment are almost at the same positions as in the full field; they might be a little closer to the center of the spot, but this could be explained by the slightly higher numerical aperture of the imaging lens due to microphones being a little higher than the loudspeakers (see Fig. 8). So, according to the Rayleigh criterion, the resolution of the confocal is not enhanced compared to the full-field scenario. Nevertheless, due to the squaring of the full-field PSF, the focal spot presents lower side lobes and a thinner spot when considering a full width at half maximum as the new criterion. By acquiring various confocal images with two scatterers separated by distances of 30 cm down to 10 cm, we can quantify the resolution of our confocal setup. At 22.5 cm, the two diffusers are almost indistinguishable (see Fig. 10), so we estimated the resolution limit in this particular imaging configuration at 22 cm.

3. Observation of the resolution enhancement in the dynamic case

In the dynamic confocal scenario, each point of the focal plane is associated with a transient wavefield. A noteworthy observation can be made from a snapshot of such a transient wavefield. Indeed, as shown in Fig. 11, the apparent wave scale in the backscattered signals is twice as small as in the focal plane.

This observation in the time domain is actually equivalent to the observations made in the main text when comparing the radial profile of the PSFs in Fig. 4. The zeros have moved closer to the center, as expected by the apparent shorter wavelength. However, the side-lobe level has come back to the same level as in the full-field scenario and is therefore higher than the confocal one.

Let us switch to a Fourier standpoint and consider the spatial frequencies transmitted by the system. The image Im_0 is built compared to the confocal one by keeping only the combination of illumination and collection wave vectors with highest NA. Each of them is limited by the diffraction to a longitudinal contribution of $1.22\lambda/(2 \text{NA})$ [see Fig. 5(a)]. This is exactly the same as in diffuse tomography [16] and leads to an enhancement in resolution by a

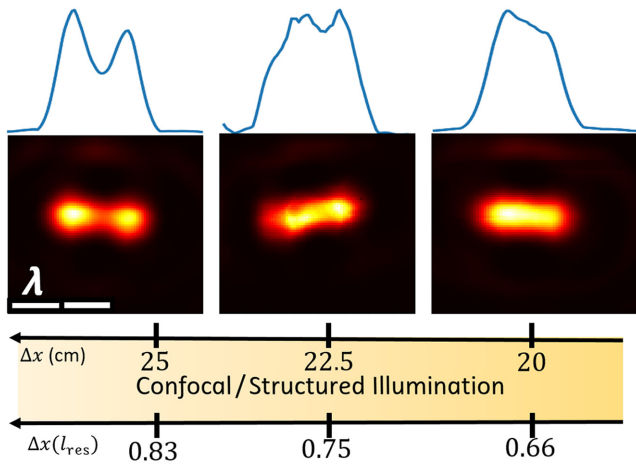


FIG. 10. Confocal images of two diffusers with various separation distances. The field of view is $90 \times 90 \text{ cm}^2$.

factor of 2. The same explanation has been proposed for structured illumination [19].

APPENDIX D: NUMERICAL ANALYSIS

All the numerical analysis is carried out using MATLAB[®].

1. Details of the numerical calculations

To write the field in the focal plane, we need to introduce the temporal Green function $G_0(\mathbf{r}, t|\mathbf{r}_s, t_0)$ relating a source at position \mathbf{r}_s emitting a Dirac at time t_0 and an observer at position \mathbf{r} in the focal plane. For scalar waves in three dimensions, it corresponds to a spherical wave function that mathematically reads

$$G_0(\mathbf{r}, t|\mathbf{r}_s, t_0) = \frac{\delta(t - t_0 - \|\mathbf{r} - \mathbf{r}_s\|/c)}{4\pi\|\mathbf{r} - \mathbf{r}_s\|}. \quad (\text{D1})$$

By applying the superposition theorem and knowing the signal emitted by each speaker, it is straightforward to numerically obtain the signal received on each point of the

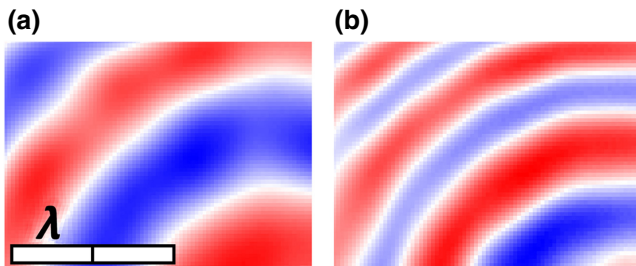


FIG. 11. Images of the temporal fields with a single diffuser. (a) In the focal plane. (b) Backscattered corresponding to the PSF acquisition. The images are extracted from a full movie where the rotation of the emission center (here at the bottom right of each image) can be observed.

focal plane since the propagation amounts to a convolution with the temporal Green function. For the sake of time efficiency, the calculations are actually performed in the Fourier domain where the convolution is a simple multiplication. We come back to the time domain at the end by applying an inverse Fourier transform.

For the backscattered step, the same procedure as in the experiment is applied. Each signal obtained in the focal plane is backpropagated by the use of the same free-space Green function toward the position of the receivers. Then, the signals are time gated in order to emulate the rotation of a receiver as in the experiment. For each position in the focal plane, we end up with a single temporal signal.

Each of these transient signals exhibits the same temporal modulation as any signal considered in the paper. Its Fourier spectrum is nonzero only on the discrete set of frequencies $\omega_0 + n\Omega$, as shown in the spectrum of Fig. 1(b) in the main text. As a consequence, it is sufficient to solely represent the data corresponding to this discrete set of frequencies.

2. Comparison with the simulation and experiment

We witness good *qualitative* agreement between the numerical analysis and the experiment both in the focal plane and the backscattered field (see Fig. 12). The phases of the vortices only differ by a constant phase factor and a constant shift. There is a slight difference in the width of the vortex rings due to some minor parameter differences in the experimental and numerical parameters that are not optimized for perfect quantitative agreement.

APPENDIX E: RECONSTRUCTION

1. Detailed procedure

The image of a single scatterer at harmonic angular frequency $\omega_0 + n\Omega$ is saved and used as the PSF_n of the system. Its inverse IPSF_n is then computed in the spatial Fourier domain using Tikhonov regularization. Typically, the following formula is applied:

$$\widehat{\text{IPSF}}_n(\mathbf{k}) = (\widehat{\text{PSF}}_n^*(\mathbf{k}) \cdot \widehat{\text{PSF}}_n(\mathbf{k}) + \sigma)^{-1} \cdot \widehat{\text{PSF}}_n^*(\mathbf{k}).$$

Even with the apodization and regularization, the level of high-frequency artifacts would be too high for each image, so a multiplying cutoff filter is added. A circularly symmetric gate window is chosen. It cuts all the spatial frequencies above $(1 + f_{\text{super}})4 \text{ NA}/\lambda$, where f_{super} is a tunable factor corresponding to the maximum possible bandwidth extension, which means superresolution.

Each image of the two scatterers is also spatially Fourier transformed and multiplied by $\widehat{\text{IPSF}}_n(\mathbf{k})$. Eventually, an inverse spatial Fourier transform allows retrieving a reconstructed image in real space, $\text{Obj}_n(\mathbf{r})$.

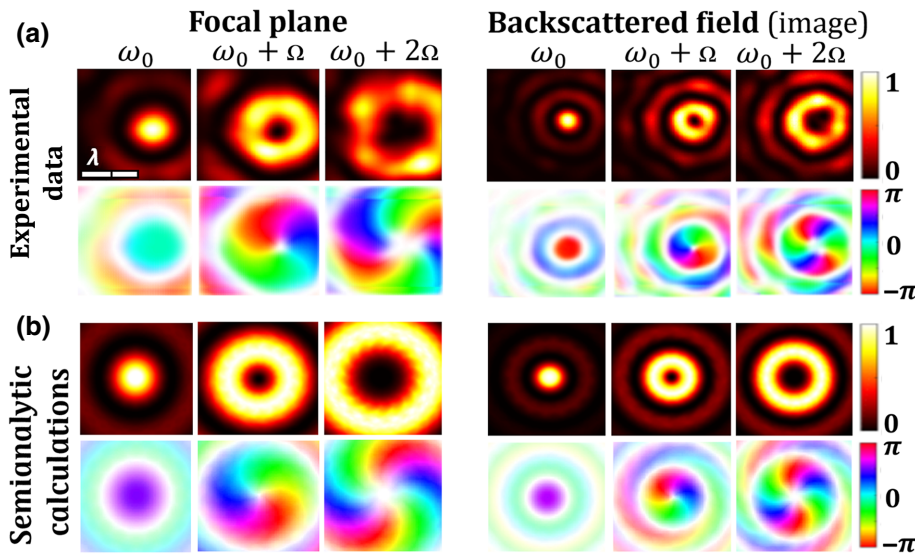


FIG. 12. Comparison of the experimental data and the simulated field. (a) Experimental data: amplitude and weighted phase spatial representation of the field in the focal plane and the backscattered field for the first four harmonic signals. (b) Semianalytic calculations data: amplitude and weighted phase spatial representation of the field in the focal plane and the backscattered field for the first four harmonic signals.

2. Choice of the reconstruction parameters

Various values for σ and f_{super} have been tried. Picking the right value is always arbitrary, like the definition of resolution criterions. To make a choice, we consider a compromise between the ability to distinguish two points

and the introduction of reconstruction artifacts. First, the superresolution factor is arbitrarily set to a value of 50%, which means a cutoff for spatial frequencies above $6 \text{ NA}/\lambda$ equivalent to a lateral resolution of 9.7 cm, which would allow us to reconstruct all the images with two scatterers.

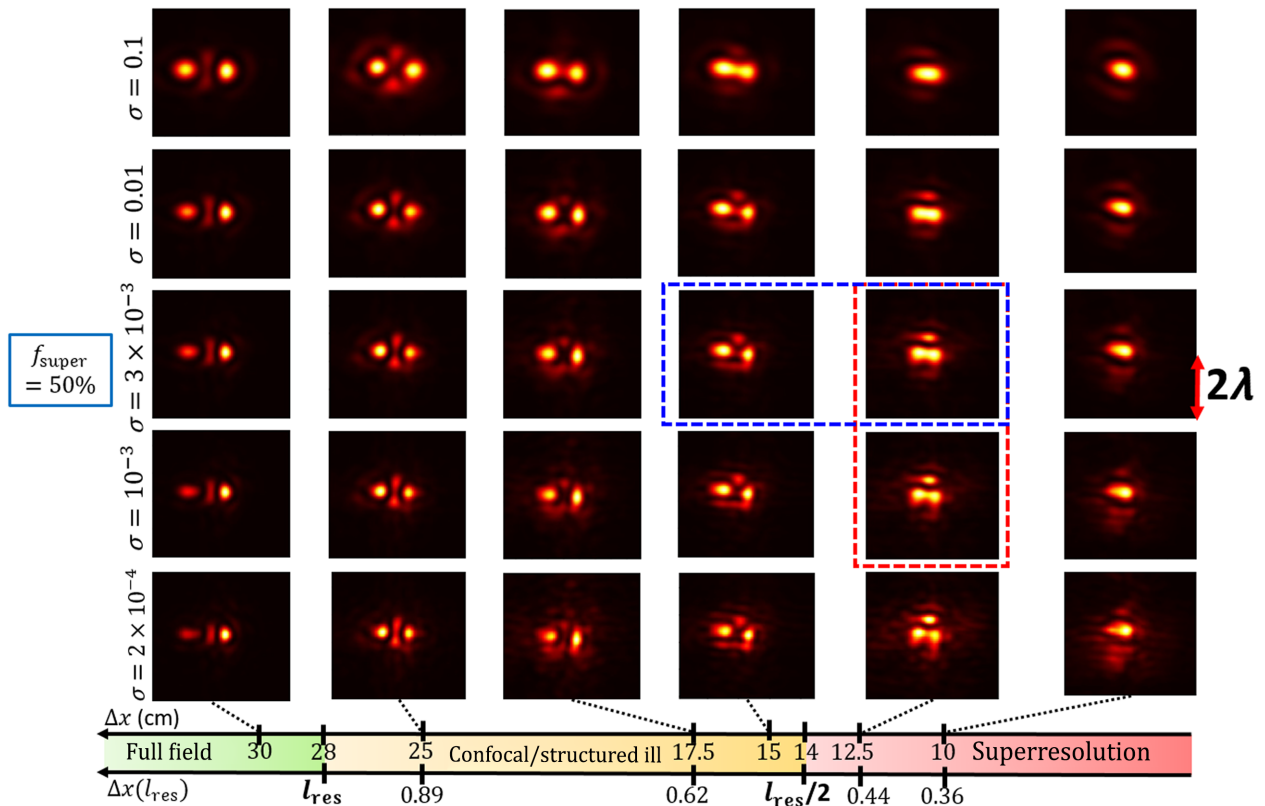


FIG. 13. Reconstructed images for various values of σ . On the first row the SNR is chosen to be low, we see that this does not allow for a good reconstruction. For the middle row ($\sigma = 3 \times 10^{-3}$) the two diffusers can be really separated for 15 cm and distinguished for 12.5 cm with reconstruction artifacts (blue box), if σ decreases again the level of artifacts becomes too high (red box).

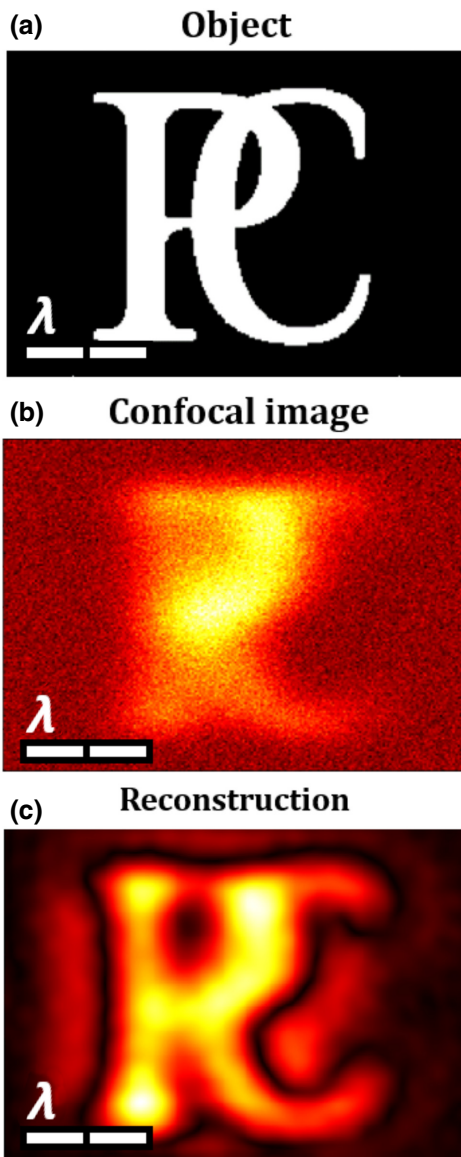


FIG. 14. Reconstruction of a continuous object. (a) The logo of *ESPCI Paris* at wavelength scale. (b) Simulated confocal image with the experimental confocal PSF. (c) Simulated reconstructed image from the dynamic images obtained with convolution of the objects with the experimental PSFs.

The inversion is then performed for different values of σ chosen on a logarithmic scale from 0.1, which is equivalent to a low signal-to-noise ratio of 10, to 1×10^{-4} . In Fig. 13 many reconstructed images are shown for various values of sigma.

The final choice ended up being a SNR of 3×10^{-3} . This value allows us to distinguish two scatterers at a 15 cm distance using the Rayleigh criterion without a high level of artifacts. It also allows us to distinguish scatterers at a distance of 12.5 cm using the *Sparrow* criterion with the presence of a small reconstruction artifact above the two scatterers. We choose not to consider a smaller value

for σ since it does not allow a significant improvement in resolution and increases the level of artifacts for this last experiment.

After this choice, attempts without success were made to increase f_{super} in order to obtain a higher lateral resolution, so the final value stayed at 50%.

3. Reconstruction of a continuous object

To be sure that our reconstruction process remains stable when the imaged sample is not sparse like in the experiment, we carry out a numerical simulation. We choose an object [see Fig. 14(a)] and convolve it with our experimental confocal PSF (black curve in Fig. 4) to get a confocal image [Fig. 14(b)]. We convolve the same object with our experimental PSFs (see Fig. 3) slightly apodized with a circular Tukey window to obtain images with a rotating illumination. We apply our reconstruction procedure with the same value of $\sigma = 3 \times 10^{-3}$ and retrieve a nicer image of the object compared to the confocal one [see Fig. 14(c)]. The resolution and contrast of the reconstructed image from simulated dynamic images seems much better than the confocal one because the high frequencies are well reconstructed using the dynamic images with vorticity.

-
- [1] E. Abbe, Beiträge zur theorie des mikroskops und der mikroskopischen wahrnehmung, *Archiv für Mikroskopische Anatomie* **9**, 413 (1873).
 - [2] L. Rayleigh, Investigations in optics, with special reference to the spectroscope, *Lond. Edinb. Dublin Philos. Mag. J. Sci.* **8**, 261 (1879).
 - [3] L. Schermelleh, A. Ferrand, T. Huser, C. Eggeling, M. Sauer, O. Biehlmaier, and G. Drummen, Super-resolution microscopy demystified, *Nat Cell Biol* **21**, 72 (2019).
 - [4] V. Astratov, *Label-Free Super-Resolution Microscopy* (Springer, Cham, Switzerland, 2019).
 - [5] Z. Liu, *Plasmonics and Super-Resolution Imaging* (CRC Press, Boca Raton, Florida, USA, 2017).
 - [6] D. Lu and Z. Liu, Hyperlenses and metalenses for far-field super-resolution imaging, *Nat. Commun.* **3**, 1 (2012).
 - [7] F. Lemoult, G. Lerosey, J. de Rosny, and M. Fink, Resonant Metalenses for Breaking the Diffraction Barrier, *Phys. Rev. Lett.* **104**, 203901 (2010).
 - [8] F. Lemoult, M. Fink, and G. Lerosey, A polychromatic approach to far-field superlensing at visible wavelengths, *Nat. Commun.* **3**, 1 (2012).
 - [9] F. Lemoult, M. Fink, and G. Lerosey, Acoustic Resonators for Far-Field Control of Sound on a Subwavelength Scale, *Phys. Rev. Lett.* **107**, 064301 (2011).
 - [10] O. Couture, V. Hingot, B. Heiles, P. Muleki-Seya, and M. Tanter, Ultrasound localization microscopy and super-resolution: A state of the art, *IEEE Trans. Ultrason. Ferroelectr. Freq. Control.* **65**, 1304 (2018).
 - [11] S. Chaudhuri, *Super-Resolution Imaging* (Springer Science & Business Media, New York, NY USA, 2001), Vol. 632.

- [12] P. Milanfar, *Super-Resolution Imaging* (CRC press, Boca Raton, Florida, USA, 2017).
- [13] M. Minsky, Microscopy apparatus, US patent 3 013 467 (1951).
- [14] R. H. Webb, Confocal optical microscopy, *Rep. Prog. Phys.* **59**, 427 (1996).
- [15] J. Mertz, *Introduction to Optical Microscopy* (Cambridge University Press, Cambridge, United Kingdom; New York, NY, 2019), 2nd ed.
- [16] O. Haerberlé, K. Belkebir, H. Giovaninni, and A. Sentenac, Tomographic diffractive microscopy: Basics, techniques and perspectives, *J. Mod. Opt.* **57**, 686 (2010).
- [17] E. Wolf, Three-dimensional structure determination of semi-transparent objects from holographic data, *Opt. Commun.* **1**, 153 (1969).
- [18] G. Zheng, R. Horstmeyer, and C. Yang, Wide-field, high-resolution Fourier ptychographic microscopy, *Nat. Photon.* **7**, 739 (2013).
- [19] M. G. L. Gustafsson, Surpassing the lateral resolution limit by a factor of two using structured illumination microscopy, *J. Microsc.* **198**, 82 (2001).
- [20] C. Roider, A. Jesacher, S. Bernet, and M. Ritsch-Marte, Axial super-localisation using rotating point spread functions shaped by polarisation-dependent phase modulation, *Opt. Express* **22**, 4029 (2014).
- [21] N. Zheludev and G. Yuan, Optical superoscillation technologies beyond the diffraction limit, *Nat. Rev. Phys.* **4**, 16 (2022).
- [22] J. W. Goodman, *Introduction to Fourier Optics* (Roberts & Company, Englewood, Colorado, 2005), 3rd ed.
- [23] J. L. Harris, Diffraction and resolving power, *J. Opt. Soc. Am.* **54**, 7, 931 (1964).
- [24] J.-B. Sibarita, *Microscopy Techniques* (Springer, Berlin, Heidelberg, Germany, 2005), Chap. Deconvolution microscopy, p. 201.
- [25] N. Ducros and A. Bourquard, Diffraction-unlimited imaging based on conventional optical devices, *Opt. Express* **28**, 11243 (2020).
- [26] S. Gazit, A. Szameit, Y. C. Eldar, and M. Segev, Super-resolution and reconstruction of sparse sub-wavelength images, *Opt. Express* **17**, 23920 (2009).
- [27] A. Szameit, Y. Shechtman, E. Osherovich, E. Bullklich, O. Sidorenko, H. Dana, S. Steiner, E. Kley, S. Gazit, T. Cohen-Hyams, S. Shoham, M. Zibulevsky, I. Yavneh, Y. Eldar, O. Cohen, and M. Segev, Sparsity-based single-shot sub-wavelength coherent diffractive imaging, *Nat. Mater.* **11**, 455 (2012).
- [28] S. Faruque, *Radio Frequency Modulation Made Easy* (Springer, Cham, Switzerland, 2017).
- [29] C. J. R. Sheppard and T. Wilson, Reciprocity and equivalence in scanning microscopes, *J. Opt. Soc. Am. A* **3**, 755 (1986).
- [30] N. Goldberg, A. Feuer, and G. Goodwin, Super-resolution reconstruction using spatio-temporal filtering, *J. Vis. Commun. Image Represent.* **14**, 508 (2003).
- [31] A. Tikhonov, Об устойчивости обратных задач [on the stability of inverse problems], *Dokl. Akad. Nauk SSSR* **39**, 195 (1943).
- [32] A. Tikhonov, Solution of incorrectly formulated problems and the regularization method, *Soviet Math. Dokl.* **4**, 1035 (1963).
- [33] S. Popoff, G. Lerosey, M. Fink, A. C. Boccara, and S. Gigan, Image transmission through an opaque material, *Nat. Commun.* **1**, 81 (2010).
- [34] P. A. Jansson, R. H. Hunt, and E. K. Plyler, Resolution enhancement of spectra*, *J. Opt. Soc. Am.* **60**, 596 (1970).
- [35] W. H. Richardson, Bayesian-based iterative method of image restoration*, *J. Opt. Soc. Am.* **62**, 55 (1972).
- [36] M. G. L. Gustafsson, Nonlinear structured-illumination microscopy: Wide-field fluorescence imaging with theoretically unlimited resolution, *PNAS* **102** (37), 13081 (2005).
- [37] M. Abramowitz and I. Stegun, *Handbook of Mathematical Functions* (National Bureau of Standards, Gaithersburg, Maryland, États-Unis, 1964), 1st ed.
- [38] M. Born and E. Wolf, *Principles of Optics* (Cambridge University Press, Cambridge, United Kingdom, 1999), 7th ed.